POLITECNICO DI TORINO
Repository ISTITUZIONALE

1D simulation models for aftertreatment components

Publisher copyright

(Article begins on next page)

20 April 2024

Chapter 11: 1D Simulation Models for Aftertreatment Components

11.1 Introduction

There are two broad and interdependent classes of choices available to minimize tailpipe emissions. One of the choices is aimed at minimization of engine out emissions through optimization of design (e.g. compression ratio, spark/injector location, in-cylinder geometry) and operating variables (e.g. EGR, valve, injection/spark timing, stoichiometry and injection shaping) [1]. However, in order to meet increasingly stringent standards, the second class of actions has to be pursued also. In this class of actions/choices, mitigating devices (i.e. aftertreatment reactors) are installed downstream of the engine, in the exhaust line. Catalytic monolith reactors are widely used in the AfterTreatment (AT) applications due to their several advantages over the conventional packed bed reactors [2]. A monolith reactor is a unitary structure usually made of ceramic or metallic material and consists of a large number of parallel flow channels with thin walls (~ 100 micron) on which a catalyst is deposited as thin layer (~10 micron). This thin layer of catalyst is usually referred as washcoat due to the catalyst deposition process. AT components can be classified into two groups based on the nature of the flow inside monolith channels: (i) flow through monoliths and (ii) wall flow monoliths. Flow through monoliths are used in Three Way Catalyst (TWC), Diesel Oxidation Catalyst (DOC), Selective Catalytic Reduction (SCR), Lean NOx trap (LNT), and Ammonia Slip Catalyst (ASC) applications. Wall flow monoliths are used in Diesel Particulate Filter (DPF) and Gasoline Particulate Filter (GPF) applications. Discussion of the catalyst technology is outside the scope of this chapter due to the limited space available and interested readers can refer to Ref [2].
An AT system will need dedicated control system in order to manage various operational requirements (e.g. Diesel Exhaust Fluid (DEF), soot regeneration, NH3 storage, etc.). Thus, especially in the concept and early design phases, it is imperative that adequate level of design and operating options are evaluated. At this point of development cycle much of the hardware may not be available for testing and, even if it were, it would likely to be prohibitively expensive. Consequently, virtual testing of design options is the only viable option and, in that, 1D simulation tools could be an effective component of the available design tools.
One of the challenges in modeling the engine AT system is to correctly represent the overlapping of several phenomena in a wide range of different operating conditions, including transient operations with complex gas mixtures. To this aim, a dedicated experimental campaign must be designed to characterize the different reaction pathways on catalysts core samples, extracted from the full-size monolith. These data are then used to calibrate kinetic parameters which are finally transferred to the full-size component model for the validation over driving cycle data, thus considering the performance of the aftertreatment system with real exhaust gas conditions as the input (Figure 11.1). Such models are essential in industrial applications, especially in the early phase of powertrain development, where they could be used for multiple purposes, including sensitivity analysis of different design parameters (PGM loading, dimensions etc.), development and optimization of control strategies, preliminary assessment of the capability of a

powertrain architecture to fulfill legislation requirements, virtual assessment of the aftertreatment system performance over real driving conditions.

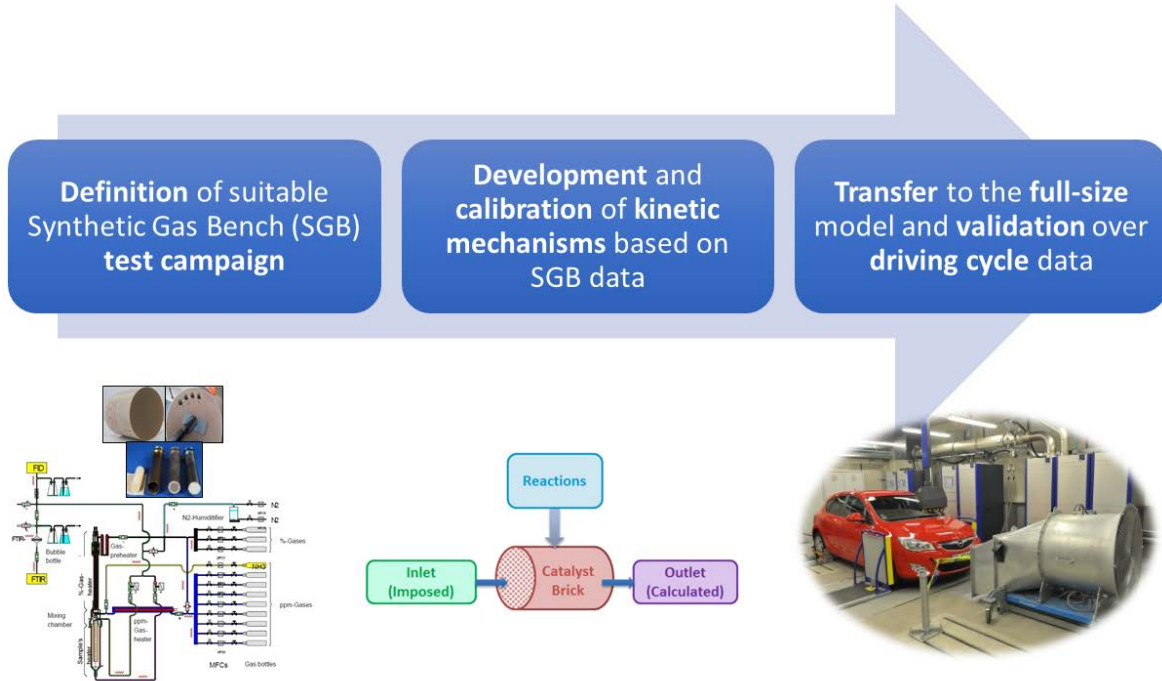In the following chapter the literature pertaining to the modeling of AT reactors is briefly reviewed.

Figure 11.1: Sample of 1D AT model development and calibration protocol, from SGB to full-size validation

11.1.1 Catalyst Technologies

Catalyst formulations used in the monoliths are tailored to a specific application and the exact composition of the catalyst is not usually disclosed by commercial catalyst suppliers. In this section, a brief overview of the commonly used catalyst technologies in the AT applications is given. Interested readers are recommended to consult the book by Gulati [2] for further details.

TWC, which oxidizes the unburned hydrocarbons and CO while simultaneously reducing NO, is used to treat the exhaust gas from gasoline engines. TWC is quite effective at stoichiometric conditions and hence gasoline engines are operated at stoichiometric conditions facilitated by a lambda sensor. Current TWC formulations contain Pt/Pd/Rh precious metals and an Oxygen Storage Component (OSC) made of Ceria/Zirconium. Due to the inherent nature of the feedback controller, the engine cannot be operated exactly with a stoichiometric mixture, therefore operates with an air-to-fuel ratio fluctuating around the stoichiometric value. TWC stores the oxygen during the lean conditions and uses the stored oxygen to oxidize HC and CO during fuel-rich operating conditions. TWC kinetics models can be found in Ref [3].

DOC is used to oxidize the unburned hydrocarbons and CO from diesel exhaust. DOC does not reduce NO like TWC but rather oxidizes it to NO_2, which could be beneficial for downstream AT components. DOC formulations commonly have Pt/Pd metals as active components and may also contain hydrocarbon absorbing materials which store unburned hydrocarbons during the cold start and release it, once reached the light-off temperature. DOC plays an important role in

the integrated emission control system, since it could serve to multiple purposes. For instance, DOC could be used to produce a specific ratio of NO_2/NO, needed for the efficient operation of downstream SCR and DPF systems. DOC kinetics models can be found in Ref [3].

LNT can be used to reduce the NOx from lean burn gasoline/diesel engines. LNT does not need an external reducing agent unlike SCR but rather depends on the engine control management for its operation. LNT stores NOx during the fuel-lean operations and engine is periodically run fuel-rich for short time to provide reducing agents which react with the stored NOx. LNT formulations have PGM, oxygen storage components such as Ceria and NOx storage components such as Barium. LNT kinetics models can be found in Ref [4].

SCR is used to reduce the NOx from the diesel exhaust gas with the help of a reducing agent. Aqueous urea solution injected at the inlet of SCR system is commonly used as a reducing agent. Based on the exhaust temperatures encountered, either vanadia- or zeolite-based catalysts are used. The zeolite catalysts are active over a wider operating temperature window than the vanadia-based catalysts but are more prone to sulfur poising. SCR kinetics models can be found in Ref [5].

ASC based on platinum (Pt) is used downstream of a SCR reactor to selectively oxidize NH_3 slipping from a SCR reactor to N_2. ASC also produces some NO which is undesirable. Dual-layered catalysts, where a SCR layer is coated on top of a Pt layer, are used to reduce the NO formation resulting in higher yield for N_2. Kinetics models for ASC can be found in Ref [6].

Particulate Filters (PF) are widely used to filter the particles produced from the engine, with efficiencies in the order of 90%. Applications of PF include Diesel Particulate Filters (DPF) and Gasoline Particulate Filters (GPF). PF are usually made of a ceramic monolith, in which the gas flow is forced through the porous walls where the filtration of particles occurs. PF are often catalyzed to accelerate the oxidation reactions of the accumulated particles, thus promoting the regeneration of the filter.

Finally, some of previously mentioned systems can also be combined in a single component, such as TWC on a gasoline particulate filter (cGPF) [7], DOC on a diesel particulate filter (CDPF or CSF) [8], or SCR on Filter (SCRoF), which combines a SCR with a DPF [5]. The combination of different components into one system enables compact design and reduced cost. However, the interaction between the catalysts and filter functions must be carefully considered. Depending on operating conditions, the effect on catalyst performance and filter functions could be promoting or detrimental [9].

11.1.1.1 Flow Through Monoliths

Figure 11.2 shows the important physical and chemical processes taking place in a washcoated monolithic reactor channel; reactants diffuse from the bulk gas phase to the washcoat surface (external mass transfer), reactants diffuse through the washcoat pores (pore diffusion), surface reactions occur at the active sites (adsorption/reaction/desorption), and finally products diffuse back through the washcoat into the bulk gas phase. Depending on the geometric, kinetic, and operating conditions, one or a combination of these steps may control the conversion rate of reactant pollutants. For example, as the inlet gas temperature increases, the controlling step may change from a kinetics-controlled regime at low temperature (before light-off) to an external mass transfer-controlled regime at high temperatures. In between these two extreme regimes a transition regime may exist, where combination of external mass transfer and pore diffusion steps control the conversion rate of pollutants. There was a substantial number of modeling

works published in the early seventies on the modeling of reactive flows in catalytic monoliths. Kuo et al. [10] were probably the first to model an automotive catalyst as a series of Continuously Stirred Tank Reactors (CSTRs), although the concept was fairly common in chemical engineering community for reactor modeling. Other works (e.g. Young and Finlayson [11]) appeared around the same time, extending the modeling to a two-dimensional domain. Heck et al. [12] published a landmark paper to demonstrate that a one-dimensional mathematical model can be sufficient to model catalytic reactions in a monolithic flow-through catalyst. Since then, an enormous amount of papers has been published in the literature, dealing on the modeling of flow through catalysts. The majority of them are focused on the development of kinetics for different catalyst formulations, while only few publications are focused on the physical processes such as heat and mass transfer coefficients and pore diffusion within the washcoat.
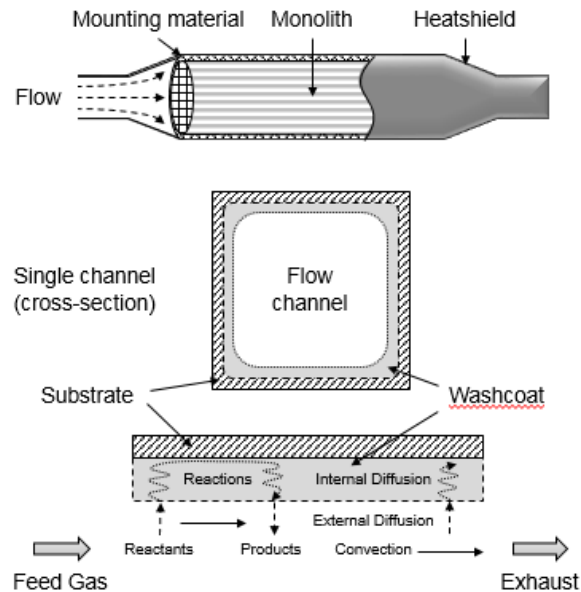

Figure 11.2: Overview of important physical and chemical processes occurring in a washcoated monolith channel

11.1.1.2 Wall Flow Monoliths

Wall Flow Monoliths (WFM) are essentially flow through monoliths with channels ends alternatively plugged, in order to force the gas flow through the porous walls, as shown in Figure 11.3, acting as filters.
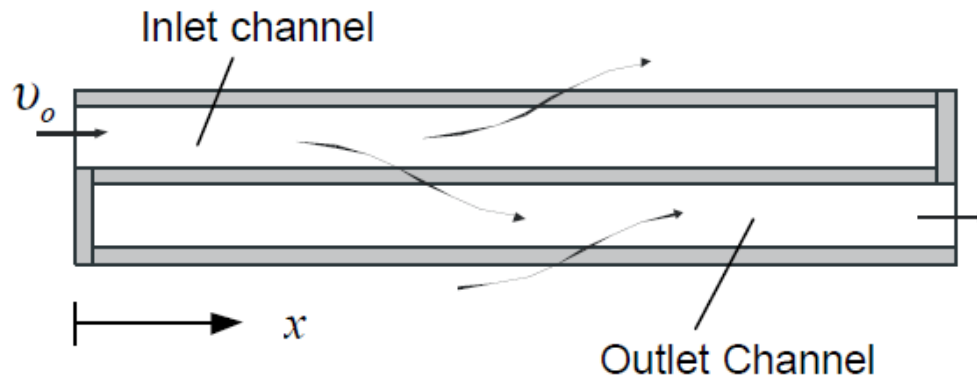
Figure 11.3: Flow pattern in a wall flow monolith [13]

This solution is very popular in AT applications to filter engine Particle Matter (PM), since the filtration efficiency of these devices could easily reach 90%. WFM are usually made by a ceramic substrate, characterized by high temperature resistance and a low thermal expansion coefficient, with pores size in the order of micrometers. On the WFM substrate, a catalyzed washcoat could be also included to accelerate oxidation reactions of the accumulated particles. Different filtration mechanisms occur in WFM. Small particles can penetrate inside the monolith pores following the gas flow streamlines. As the particle approaches a wall, it is collected on the surface because of Brownian inertia. This regime of filtration is called deep bed or depth filtration, as shown in Figure 11.4. Once pores are saturated, particles start to accumulate on the external surface (cake filtration regime, Figure 11.4). As this external layer becomes thicker, the pressure drop across the monolith increases, thus the filter must be periodically regenerated.
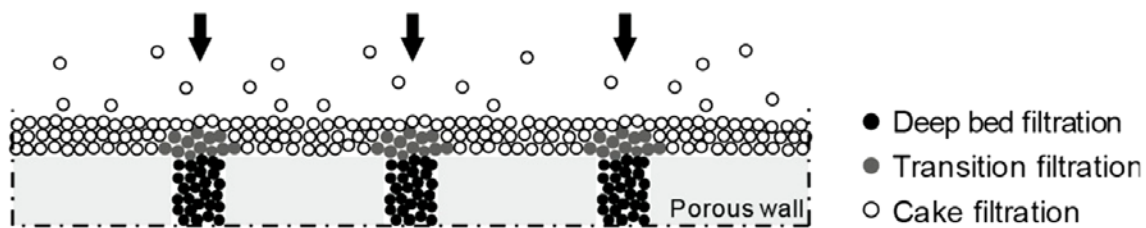

Figure 11.4: Filtration mechanisms in a wall flow monolith [14]

From a modeling point of view, WFM phenomena involve different length scales. A first class of models describes the operations occurring at the macroscopic level of the entire filter scale. The second class of models describes the filter channels length scale while the third one models the phenomena occurring at the microscopic scale of the soot layer and the porous filter walls [15]. A comprehensive review of many scales of DPF systems and the corresponding models can be found in reference [16]. In the recent decades, the combination of different catalysts with the WFM has become an important application in the emission control of both gasoline and diesel systems. In particular, combining DOC catalyst with a diesel particulate filter (CDPF) could reduce the balance point temperature by more than 100 degrees which leads to partial filter regenerations at low temperatures and less frequent fuel-consuming forced regeneration due to post-injection [9]. Another important integrated system is the combination of filter functions and

DeNOx capabilities with SCR catalyst, i.e., the so called SCRF or SDPF system. Due to the interaction of NOx reduction and soot oxidation reactions, the design and control of a SCRF system needs to balance between DeNOx performance, filtration efficiency and pressure drop behaviors [17]. A detailed review of the evolution and most recent developments in catalyzed DPF modeling can be found in reference [9].

11.2 Mathematical Model for Flow Through Monoliths

The mathematical model describing the physical and chemical processes shown in Figure 11.2 can be formulated with the following assumptions: (i) conduction and diffusion in the flow direction are negligible in the bulk phase due to high space velocities encountered in these reactors, (ii) laminar flow is assumed in the channel due to low Reynolds numbers (< 1000), (iii) uniform cross sectional area is considered, (iv) reactions occur only in the washcoat (i.e. homogeneous gas phase reactions are negligible), (v) transverse temperature gradients in the solid phase are negligible compared to axial gradients, (vi) a uniform radial distribution of the gas at the front face is assumed, while channel to channel variations and interactions are ignored, (vii) transversal gradients are accounted using heat and mass transfer coefficients between the fluid and solid.

The last two assumptions allow to simplify the 2D/3D models into a 1D model where a single representative channel can be used to describe the entire monolith reactor. With the above assumptions, the mathematical model (referred here as $1 + 1D$ model due to one spatial dimension in the flow direction and second spatial dimension through the washcoat thickness) is described by the following conservation equations and boundary conditions:

Gas phase species:

$$f_{vd}\rho_g \frac{\partial \omega_{g,i}}{\partial t} = -f_{vd}\rho_g u \frac{\partial \omega_{g,i}}{\partial z} - \rho_g k_i S \left(\omega_{g,i} - \omega_{s,i}\right) \tag{11.1}$$

Gas phase energy:

$$f_{vd}\rho_g C_{pg} \frac{\partial T_g}{\partial t} = -f_{vd}\rho_g C_{pg} u \frac{\partial T_g}{\partial z} + h\, S\left(T_s - T_g\right) \tag{11.2}$$

Solid phase energy:

$$\psi_s \frac{\partial T_s}{\partial t} = \frac{\partial}{\partial z}\left(\Lambda_s \frac{\partial T_s}{\partial z}\right) - h\, S\left(T_s - T_g\right) - h_x\, S_x (T_s - T_x) + \sum_{l=1}^{2} \sum_{n=1}^{n_{rxns}} \Delta H_n^{(l)} a_n^{(l)} \bar{r}_n^{(l)} \tag{11.3}$$

Where Λ_s and ψ_s are, respectively, effective thermal conductivity and effective heat capacity of solid phase, and are given by the following equations:

$$\Lambda_s = f_{sb}\lambda_{sb} + \sum_{l=1}^{2} f^{(l)}\lambda^{(l)} \qquad (11.4)$$

$$\psi_s = f_{sb}\rho_{sb}C_{p,sb} + \sum_{l=1}^{2} f^{(l)}\rho^{(l)} C_p^{(l)} \qquad (11.5)$$

$\bar{r}_n^{(l)}$ is the average reaction rate across the effective washcoat thickness:

$$\bar{r}_n^{(l)} = \frac{1}{\delta^{(l)}} \int_0^{\delta^{(l)}} r_n^{(l)} \, dx \qquad l = 1, 2 \qquad (11.6)$$

Where the effective washcoat thickness is defined as:

$$\delta^{(l)} = \frac{f^{(l)}}{S}, \qquad l = 1,2 \qquad (11.7)$$

The effective washcoat thickness defined as above accounts for the small additional washcoat volume in the corners of a channel and will be slightly larger than the measured value. Initial and boundary conditions for the above differential equations are trivial and are not given here. The following equations present the species balances and boundary conditions in the washcoat layers. Washcoat species:

$$f^{(l)}\varepsilon^{(l)}\rho_s \frac{\partial \omega_i}{\partial t} = f^{(l)}\rho_s D_{i,eff}^{(l)} \frac{\partial^2 \omega_i}{\partial x^2} + R_i^{(l)}, \quad l = 1, 2 \qquad (11.8)$$

$R_i^{(l)}$ is the ith species rate in layer l:

$$R_i^{(l)} = MW_i \sum_{n=1}^{n_{rxns}} s_{i,n} a_n^{(l)} r_n^{(l)} \qquad (11.9)$$

Boundary condition at the surface:

$$k_{m,i}\rho_g\left(\omega_{g,i} - \omega_{s,i}\right) = -\rho_s D_{i,eff}^{(1)} \frac{\partial \omega_i}{\partial x}\bigg|_{x=0} \qquad (11.10)$$

Flux continuity at the layer interface:

$$\rho_s D_{i,eff}^{(1)} \frac{\partial \omega_i}{\partial x}\bigg|_{x=\delta^{(1)}-} = \rho_s D_{i,eff}^{(2)} \frac{\partial \omega_i}{\partial x}\bigg|_{x=\delta^{(1)}+} \tag{11.11}$$

Boundary condition at the bottom of the washcoat:

$$\frac{\partial \omega_i}{\partial x}\bigg|_{x=\delta^{(1)}+\delta^{(2)}} = 0 \tag{11.12}$$

Site balance:

$$A_k^{(l)} \frac{\partial \theta_k^{(l)}}{\partial t} = \sum_{n=1}^{n_{rxns}} \sigma_{k,n} a_n^{(l)} r_n^{(l)} \quad l = 1,2 \tag{11.13}$$

The reaction rates used in the above equations are based on the turnover number, defined as the ratio of moles reacted per moles of active sites per second. Volume rates are obtained by multiplying turnover rates with the active site density. The site density indicates the ratio between moles of active sites (PGM sites, storage sites etc.) and the catalyst volume, acting as a kinetics scaling factor for different catalyst loadings. It is recommended to use turnover rates as they are independent of catalyst loading and hence are easily portable to different reactors with same catalyst formulation but different catalyst loadings. Turnover rates are also useful when modeling aging and poisoning of catalysts, which are generally accounted for by reducing the active site density, allowing the distinction between an ideal case (all the sites are active) and the real case (only some of the sites are active).
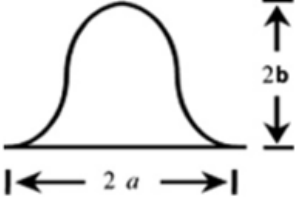
11.2.1 Heat and Mass Transfer Coefficients

Heat and mass transfer coefficients determine the rate of heat and mass transfer from fluid to solid walls and are calculated from dimensionless Nusselt and Sherwood numbers, which depend on the channel geometry and on the flow conditions inside the channel. Ideally, their values should be determined from experiments but, due to the uncertainty of experimental data, they are typically derived from the analogy with heat transfer problems. It is important to use appropriate values for these coefficients during the simulations as they determine the conversion efficiency in the external mass transfer-controlled regime. When the boundary layers (flow, thermal, and concentration) are fully developed, Nusselt and Sherwood numbers assume asymptotic/constant values specific to channel geometry and wall boundary conditions, as given in Table 11.1. These asymptotic values are obtained as a solution to the classical Graetz-Nusselt problem with constant flux or constant temperature boundary condition. Values approach the constant flux limit (Nu_{H2}/Sh_{H2}) when the reactions are slow (before light-off) and approach the constant temperature limit (Nu_T/Sh_T) when the reactions are fast (after light-off).
The gas flow rates encountered in the AT reactors are such that the Reynolds number based on channel diameter is usually in the range 100-1000. Since the dimensionless flow development length (L_h/D_h) for laminar flow in a channel is of the order of 0.05 Re, the entrance length could

vary from 5 to 50 times the channel hydraulic diameter. When the boundary layer development lengths are significant, it is essential to use position-dependent heat and mass transfer coefficient values, instead of constant asymptotic values. There is a vast amount of literature, spanning the past four decades and dealing with both theoretical and experimental aspects, on heat and mass transfer coefficients in laminar flows for reacting as well as non-reacting cases. Gundlapally and Balakotaiah [18] compared several different popular correlations and also analyzed the effect of coefficients on the performance of monolith reactors. It was shown that, when the transverse Peclet number ($P = \frac{uD_h^2}{16LD_{m,i}}$) is less than 0.25, flow conditions in the entry region of a monolith channel have negligible effect on the exit conversion. Normally, the transverse Peclet number is less than 0.1 for the monoliths used in the automotive exhaust aftertreatment applications and hence the constant values reported in Table 11.1 can be used in practical applications, instead of the position dependent correlations.

Table 11.1: Asymptotic values of Nusselt/Sherwood numbers and friction factors for commonly used channel geometries [18]

Channel shape	$D_h(4R_\Omega)$	$(f\,Re)_\infty$	$Nu_{H2\infty}(Sh_{H2\infty})$	$Nu_T(Sh_T)$
	$2a$	16	4.364	3.656
	$2a$	14.23	3.089	2.977
	$1.5419a$	14.574	0.95	2.496
	$1.418a$	14.023	1.38	2.536
	$1.2103a$	13.023	1.55	2.476
	$1.0466a$	12.234	1.34	2.353
	$0.8118a$	11.207	0.90	2.110
	0.4673	10.123	0.33	1.719

11.2.2 Bulk and Effective Diffusion Coefficients:

There are several correlations available in the literature for calculating molecular diffusion coefficients in binary mixtures. Two correlations that are widely used are the Chapman-Enskog [19] correlation and Fuller correlation [20]. The Chapman-Enskog correlation is:

$$D_{i,j} = \frac{1.858 \times 10^{-7} T^{1.5} \sqrt{\frac{1}{MW_i} + \frac{1}{MW_j}}}{P\sigma_{i,j}^2 \Omega_D} \tag{11.14}$$

Where Ω_D is the collision integral, and $\sigma_{i,j}$ is the force constant. The values of Ω_D and $\sigma_{i,j}$ for many species can be found in Ref [21].

The fuller correlation is based on special atomic diffusion volumes [20] and is given by

$$D_{i,j} = \frac{10^{-7} T^{1.75} \sqrt{\frac{1}{MW_i} + \frac{1}{MW_j}}}{P \left((\Sigma_i v_k)^{\frac{1}{3}} + (\Sigma_j v_k)^{\frac{1}{3}} \right)^2}$$ (11.15)

where T is the temperature (K), P is the pressure (atm), MW is the molecular weight (g/mol), and v_k is the atomic diffusion volume (cm^3) summed over all the atoms contained in the diffusing species. The mixture-averaged diffusion coefficient $D_{i,m}$ is calculated from the above binary diffusion coefficients $D_{i,j}$

$$D_{i,m} = \frac{1 - \omega_i}{\sum_{\substack{j=1 \\ j \neq i}}^{nsp} \frac{X_j}{D_{i,j}}}$$ (11.16)

Effective diffusion coefficients within the washcoat can be estimated using either the parallel pore model or random pore model. The parallel pore model is widely used for its simplicity. Using the parallel pore model, effective diffusion coefficient is estimated from the mixture-averaged diffusion coefficient, Knudsen diffusion coefficient $D_{i,kn}$, and washcoat properties as:

$$D_{i,eff}^{(l)} = \frac{\tau^{(l)}}{\varepsilon^{(l)}} \left(\frac{1}{D_{i,m}} + \frac{1}{D_{i,kn}^{(l)}} \right)$$ (11.17)

$$D_{i,kn}^{(l)} = \frac{d_p^{(l)}}{3} \sqrt{\frac{8R_g T}{\pi MW_i}}$$ (11.18)

Where $\tau^{(l)}$, $\varepsilon^{(l)}$, and $d_p^{(l)}$ are tortuosity, porosity, and pore diameter of washcoat layer l, respectively. The molecular weight of species i, MW_i, is expressed as (kg/mol) in the above equation.

It should be noted that the structure of the washcoat could be highly complex, with many different sizes of pores interconnected with tortuous paths. As such, it would not be realistic to expect high degree of accuracy with simple models like parallel pore or random pore models, while using average washcoat properties (i.e. pore diameter, tortuosity, and porosity). Usually, the average pore diameter reported by catalyst suppliers is in the order of nanometers, which

results in small values for effective diffusivities using the above formulas. It is important to check that the estimated effective diffusivities have the same of order of magnitude as the measured diffusivity values. Figure 11.5 shows the bulk and effective diffusion coefficients of selected species, in a nitrogen atmosphere, as a function of the temperature. Using $\tau^{(l)} = 3, \varepsilon^{(l)} = 0.4, and\ d_p^{(l)} = 5\mu m$, the calculated effective diffusion coefficients are on the order of $10^{-6}\ m^2/s$, which are close to the values measured in Ref [22].
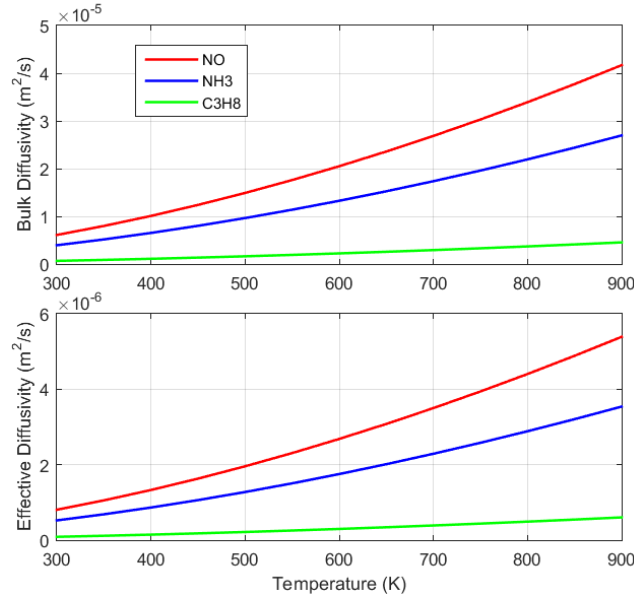

Figure 11.5: Bulk and effective diffusion coefficients of selected species as a function of temperature [33]

11.2.3 Extending 1D framework to 2D/3D

As pointed out earlier, assuming uniform gas flow across the front of the reactor and neglecting channel to channel interaction allows to use only one channel as representative of the entire monolith [23]. If these conditions are not satisfied, the non-uniform gas distribution at the reactor inlet and channel to channel interactions via conduction should be considered. For example, as shown in Figure 11.6, NH3 concentration near inlet of a SCR reactor may not be uniform due to the complex processes of injection, decomposition, wall deposition and evaporation. 1D modeling framework can be extended to account for these affects. Instead of solving a single channel, bundles of thermally interacting channels (via conduction), strategically arranged in the 3D space, can be used as an alternative to full 3D CFD simulations [23].
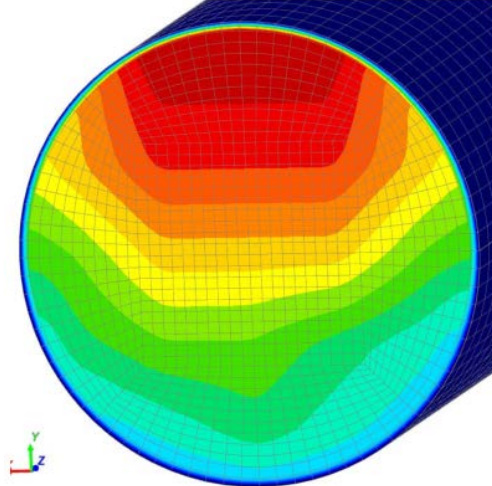
Figure 11.6: simulated NH3 distribution at the front face of an SCR

11.2.4 Pore Diffusion

Numerically coupling the washcoat diffusion-reaction equation (Eqn. 11.7) with 1D equations at each axial location is computationally expensive. The simplest approach to avoid the computational cost of a full numerical solution is to neglect the pore diffusion resistance. In the absence of pore diffusion resistance, species concentration profiles in the washcoat are constant. By integrating the diffusion-reaction equation (Eqn. 11.7), using boundary conditions as in Eqns. 11.9 and 11.11, will result in the following equation, expressing the concentration in a single layer washcoat

$$f^{(1)}\varepsilon^{(1)}\rho_s \frac{d\omega_{s,i}}{dt} = S\rho_g k_i\left(\omega_{g,i} - \omega_{s,i}\right) + R_i^{(1)}(\boldsymbol{\omega_s}) \tag{11.19}$$

where $\omega_{s,i}$ is the surface concentration of species i. Even though this is a reasonable approximation for the aftertreatment applications, as the washcoat layers are generally thin and highly porous, the interest in understanding the effect of pore diffusion remains strong, especially for dual layer catalysts, where pore diffusion resistance is intentionally exploited to achieve a higher conversion efficiency [21,24–26]. Thus, simplified approaches involving the effectiveness factor [27], the internal mass transfer coefficient [28–30] and the asymptotic solution [31,32] are proposed to capture the effect of pore diffusion resistance without the significant computational cost associated with the full numerical solution. For example, Figure 11.7 shows the comparison of asymptotic solution with 1 + 1D solution for the species concentration profiles within a dual layer washcoat of a SCR reactor [33].
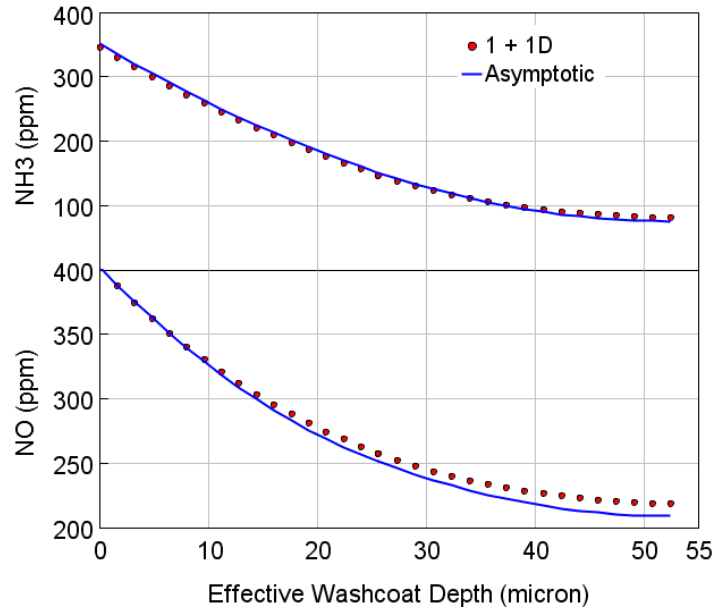
Figure 11.7: NH₃ and NO emissions vs Effective Washcoat Depth, comparison between 1+1D and Asymptotic solution approaches [33]

11.2.5 Numerical Solution

The Method of Lines (MOL) approach is widely used in the literature to discretize the Partial Differential Equations (PDEs) presented in the section 11.2. After discretizing the spatial dimension, the PDEs become ordinary Differential Equations (ODEs) which can be solved using any of the ODE solver packages available in the open literature. The most popular ODE solver packages like LSODI, VODE, and DASPK are based on implicit Backward Difference Formulas (BDF), which are best suited for the stiff problems encountered in aftertreatment reactors. Note that the diffusion-reaction equation (Eqn. 11.7) also need to be discretized along the washcoat thickness for the full numerical solution of the 1 + 1D model. This increases the computational cost tremendously as additional variables (for species concentrations), at the transverse mesh points within the washcoat, need to be solved at each axial mesh point.
It should be noted that there exist some commercial software packages that are customized for modeling of AT reactors. These commercial packages automatically formulate and discretize the above differential equations given the user input of reactions mechanism, geometry, and operating conditions. One of the important input parameters for the ODE solvers are the error tolerances, which must be set judiciously for the optimum performance of ODE solvers. Using error tolerances that are too loose may lead to an incorrect solution or to solver failures, whereas the use of too stringent tolerances may degrade the performance of solver. It is recommended to run the simulations with different tolerances to assess the impact on the solution and to optimize the solver performance. For species fractions, absolute tolerance of 10^{-6} (1 ppm) could be used as a starting point. The absolute tolerance can be set to zero for temperatures as their magnitude will be much larger than zero and hence relative tolerance becomes the controlling parameter. A relative tolerance of 10^{-3} could be used as starting value for species fractions and temperatures.

11.2.6 Quasi-steady state approximation

The Quasi-Steady-State (QSS) approximation is widely used by the reactor modeling community because it reduces the computational time by eliminating shorter time scales associated with the small accumulation terms (time derivatives) in the gas phase species, energy, and washcoat species balance equations. The system of PDEs discussed above becomes a system of Differential Algebraic Equations (DAEs), after invoking the QSS approximation. It is important to note that the QSS approximation introduces additional mathematical complications when the surface concentration changes discontinuously along the reactor length. It will briefly discussed here why the so-called concentration jumps cause the DAE solver failures, while interested readers could refer to Ref [34] for more information on nonlinear dynamic analysis of catalytic reactors. To simplify the discussion, the pore diffusion resistance in the washcoat will be neglected here. For this limiting case, Eqn. 11.13 becomes the following algebraic equation, after applying the QSS assumption:

$$S \, \rho_g \, k_i \left(\omega_{g,i} - \omega_{s,i} \right) + R_i(\boldsymbol{\omega_s}) = 0 \tag{11.20}$$

Discontinuities in the surface concentration, ω_s, occur when the solution to the above algebraic equation reaches a limit point, where the Jacobian matrix becomes singular. At the limit point, the surface concentration undergoes abrupt changes. Figure 11.8 shows bulk and surface CO concentration profiles along the channel length, where it can be noticed that the discontinuity in the CO surface concentration occurs at the dimensionless channel location of 0.5, where the surface concentration jumps from 0.25% to 0.04%. DAE solvers struggle as the solution approaches the discontinuity and often fail as the error test forces very small time-step sizes. Thus, special considerations have to be taken during the simulation to avoid integration failures due to concentration jumps. The Jacobian matrix must be monitored and a special logic should be adopted to help the DAE solvers in finding the solution at the limit point. The rest of the variables ($\boldsymbol{\omega_g}, T_g$) do not change discontinuously because axial derivative terms that appear in the governing equations guarantee smoothness.
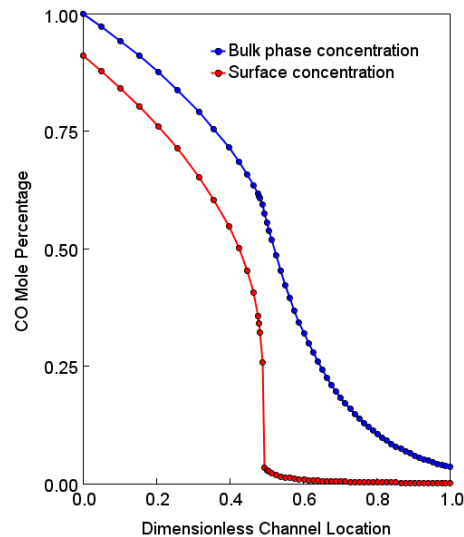
Figure 11.8: Bulk and surface concentration profiles. Surface concentration profile shows an abrupt change in CO concentration at the dimensionless channel location of 0.5 [33]

11.2.7 Adaptive mesh

Sharp reaction fronts where most of the reactant conversion takes place are routinely present inside the channels of monolith reactors. These reaction fronts dynamically move within the channel in response to the operating conditions and accurately resolving species concentration profiles inside a reaction front is computationally challenging. An adaptive meshing method that dynamically follows the reaction fronts was proposed in Ref [35] but this method has not seen wide spread use in the simulation of aftertreatment reactors. An adaptive mesh with little computational overhead can be implemented since the solid temperature and surface coverages vary slowly with time due to their large accumulation or capacity terms whereas species concentrations and gas temperature exhibit fast dynamics due to their small accumulation terms. After applying the QSS assumption, solid temperature and coverage equations are the only equations that have explicit time derivatives, while species and gas temperature equations have only axial derivatives. Thus, it is possible to construct the problem as inner and outer integration problems. In the outer problem, time integration of solid temperature and coverages is carried out on a fixed uniform MOL mesh whereas in the inner problem integration of DAE system consisting of species and temperature equations is carried out. In this dual mesh strategy DAE solver automatically creates the spatially non-uniform mesh in accordance with the specified error tolerances. It should be noted that this approach does not decouple or lag the variables in any way but simply takes advantage of the particular structure of the PDE system [35].
The first significant and obvious advantage of the above adaptive mesh technique over the fixed uniform mesh is that the adaptive mesh dynamically adjusts with the moving reaction front inside the channel. The second significant advantage lies in the automatic control of axial integration errors in addition to the time integration errors, whereas with the standard solution methods only time integration errors are controlled. This feature results from the decomposition of the problem into time and axial integration problems. With a non-adaptive mesh, the accuracy of the solution must be accurately checked by varying grid resolution, ensuring that the obtained solution is grid-independent, whereas the adaptive meshing technique discussed above dynamically refines the axial mesh resolution for grid-independent solution. This is illustrated in Figure 11.9, which shows the comparison of axial CO bulk gas phase concentration profiles obtained using both the adaptive and fixed mesh points. It can be seen that a finer mesh is needed when using fixed mesh to match the results of adaptive mesh. In this particular example, the fixed mesh solver needs more than three times axial mesh points than the adaptive mesh to obtain the grid-independent solution.
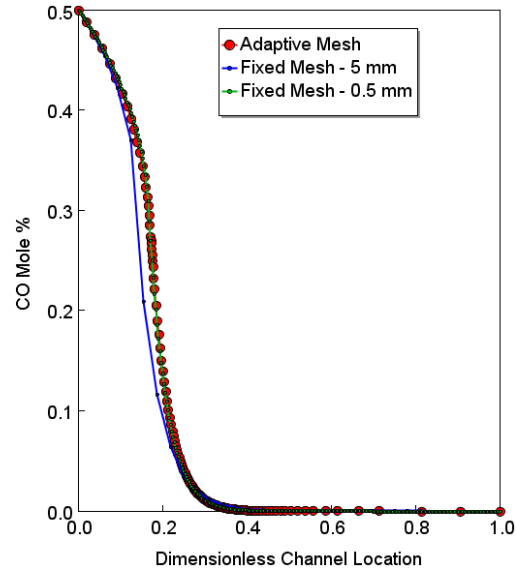
Figure 11.9: CO concentration profiles demonstrating the advantage of automatic control of the axial integration errors [33]

11.3 Mathematical Model for Wall Flow Monoliths

Both diesel and direct injection gasoline engine produce particulate matter as a product of the combustion. The amount of tail-pipe emissions depends on the engine operating/design variables and on the mitigating steps taken at the exhaust system. The presence of particulate filter in the exhaust system affects the engine performance in many ways. First, it increases the exhaust back pressure, as more soot particles are collected in the filter. Therefore, the filter must be periodically regenerated by burning the stored particles. Thus, additional fuel must be injected to initiate the filter regeneration, increasing the engine fuel consumption. In this context, mathematical models of particulate filters can be effective in supporting the development of efficient control systems and the whole system design processes.

In order to fully understand design tradeoffs, a physics-based model is needed. The first of such mathematical models was proposed by Bissett [36], which included the conservation equations for mass, energy and momentum, for both inlet and outlet channels. Channels were coupled through a uniform flow from inlet to outlet, while a constant inlet channel diameter was assumed, regardless of soot cake formation. The deep bed filtration regime was neglected in the model, while the soot cake formation was considered. Nevertheless, the model was remarkably successful and formed the basis of subsequent model improvements.

Successive generation of models added various features such as the deep bed filtration, based on the spherical unit collector model [23]. Konstandopoulos and Johnson [37] compared three types of filtration models; the fibrous filter model, the spherical unit collector model and the periodically constricted tube model. The spherical unit collector model was chosen due to the consideration of computational cost, to the estimation of input parameters and to the similarity between the model and the monolith wall structures. Several related works incorporated diffusion of oxygen [38] as well as so called back diffusion of NO_2 [39] and NO_2 assisted soot kinetics [40]. Due to the diffusion in the soot cake and substrate layers, species concentration varies along the channel length. Within the practical application range of a WFM, the soot cake

thickness can be neglected compared to the channel width. Then the species equations in the channels can be written as [41]:

$$\rho_1 v_1 \frac{\delta y_{1,j}}{\delta z} = \rho_1 k_{1,j} \frac{4}{D_1} \left(y_{w1,j} - y_{1,j}\right) - \rho_{w1} v_{w1} \frac{4}{D_1} \left(y_{w1,j} - y_{1,j}\right) \tag{11.21}$$

$$\rho_2 v_2 \frac{\delta y_{2,j}}{\delta z} = \rho_2 k_{2,j} \frac{4}{D_2} \left(y_{w2,j} - y_{2,j}\right) - \rho_{w2} v_{w2} \frac{4}{D_2} \left(y_{w2,j} - y_{2,j}\right) \tag{11.22}$$

The species equation in the soot cake and substrate is:

$$\rho_w v_w \frac{\delta y_j}{\delta x} - \rho_w D_{eff,j} \frac{\delta^2 y_j}{\delta x^2} = R_j \tag{11.23}$$

The conservation equations for the mass, momentum and energy can be written as:

$$\frac{\delta(\rho_i v_i)}{\delta z} = (-1)^i \frac{4}{D_i} \rho_{wi} v_{wi} \tag{11.24}$$

$$\frac{\delta p_i}{\delta z} + \beta \frac{\delta(\rho_i v_i^2)}{\delta z} = \frac{2C_f Re}{D_i^2} \mu_i v_i \tag{11.25}$$

$$\rho_i v_i C_{p,i} \frac{\delta T_i}{\delta z} = h_i \frac{4}{D_i} \left(T_{w,i} - T_i\right) + (-1)^{-i} \frac{4}{D_i} \rho_{wi} v_{wi} \left(T_{w,i} - T_i\right) \tag{11.26}$$

Where $i = 1$ (inlet channel), 2 (outlet channel). Based on Bissett [42], the friction factor $C_f Re$, the momentum flux factor β and the Nusselt/Sherwood numbers are functions of the wall Reynolds number. There is an interesting observation that could be made by looking at the balance equations for the inlet channel. This is most recognizable in the energy equation term when expressed in nondimensional form:

$$Pe_w \hat{v}_{z,av} \frac{d\hat{T}}{d\hat{z}} = (Nu - Pe_w)(1 - \hat{T}_b) \tag{11.27}$$

It can be seen that, for a fixed Nusselt number, there exists a wall Peclet number above which the gas temperature in the channel increases with wall cooling, which might result counter intuitive other than unphysical. To address this issue, Koltsakis and Stamatelos [43] wrote the inlet channel gas energy equation by assuming that the gas leaves the channel at the bulk gas temperature T_1, which is different from the approach taken for the outlet channel in which gas enters the control volume at wall temperature T_w. This assumption removed the possibility of unphysical temperature gradients.

$$C_{p,g}\rho_1 v_1 \frac{\delta T_1}{\delta z} = h_1 \frac{4}{d_1}(T_w - T_1) \qquad (11.28)$$

$$C_{p,g}\rho_2 v_2 \frac{\delta T_2}{\delta z} = (h_2 + C_{p,g}\rho_w v_w)\frac{4}{d}(T_w - T_2) \qquad (11.29)$$

A similar assumption was also adopted in the species equations and in the corresponding boundary conditions. However, Bissett et al. [42] took a different approach. They identified that the use of constant Nusselt number was the cause of the non-physical behavior of the governing equation. In fact, it was a common practice to use the Nusselt number of a non-porous wall square channel for the porous wall flow monoliths. Bissett et al. [42] found that Nusselt number and friction coefficients are sensitive functions of the wall Reynolds number and, specifically, that there is a non-monotonic behavior in the inlet channel. It can be seen in Figure 11.10 that the regime of the non-physical Peclet number (denoted by the dashed line) is never reached.
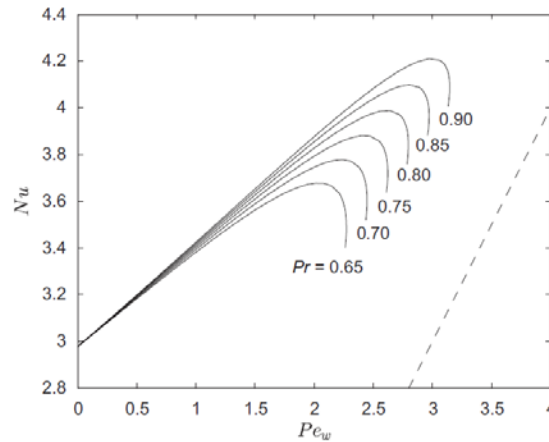

Figure 11.10: Nusselt number in square inlet channel [42]

The above work was further extended by Wang et al. [44] for other geometries of the porous channels. In order to extend the life span of the monoliths and to maintain low pressure drops with soot and ash loading, other channel shapes other than square, such as triangle, hexagon or octa-square, have been studied in the literature. Particularly, it has been shown that the hexagon channel design [45–47] could increase the regeneration efficiency and the soot oxidation rate compared to the conventional square channel designs. For hexagon channel monoliths, there are two inlet channels for each outlet channel. When there is no soot cake or the soot loading is small, the pressure drop of hexagon channel WFMs is shown to be higher than the square channel monoliths [47] as flow mainly goes through the walls between the inlet channel and outlet channels. However, when the soot cake formation was observed on the walls between two inlet channels, in medium or high soot loading regimes, hexagon channel WFMs showed a lower pressure drop than square channel monoliths.

In Wang and Bissett [44], the friction factors and Nusselt numbers correlation for triangle and hexagon channels with porous walls are derived by solving the three-dimensional (3D) incompressible flow problem. A similar solution has been adopted for the fully developed flow and heat transfer problem, in triangle and hexagon channels with wall suction and injection. Different flow patterns are observed between the symmetric and asymmetric hexagon channels,

yet the integrated flow characteristics such as overall friction coefficients and Nusselt numbers are shown to be insensitive to the symmetry of boundary conditions. Figure 11.11 shows the streamlines in one-sixth of a hexagon suction channel with the symmetric and asymmetric boundary conditions (BCs). The symmetric BC corresponds to the medium or high loading regime while the asymmetric BC corresponds to clean or low loading regime. Figure 11.12 compares the overall friction factors of the two types of channels. The simulation results for each geometry are fitted into polynomial and limit-point functions. For reader's reference, the fitting functions are listed in Table 11.2 through 11.7. The advantages of polynomial function fitting lie in its simplicity and in the fitting accuracy, which can be improved by increasing the order of the functions. On the other hand, the limit-point function fitting shows better accuracy in proximity of the critical wall Reynolds number, $Re_{w,c}$. In addition, the limit-point function fitting generally shows less error than the polynomial function fittings using the same or fewer coefficients. With results for several geometries available, it is natural to ask which geometry is better, at least in terms of flow resistance. A comparison of the $C_f Re$ values for all the geometries is depicted in Figure 11.13 (a). However, it should be noted that for this comparison, the wall velocity and the hydraulic diameter are assumed to be constant for all the analyzed geometries. For a more practical comparison, it must be considered how the channels are combined into the WFM, since the result might sensitively depend on additional properties of the monolith and on the parameters that are held constant between different geometries. In Wang and Bissett [44], an example of such comparison was shown, by assuming that the temperature, the total mass flow rate and the overall monolith geometry (such as frontal area and length) are held constant for different geometries. In addition, it was assumed that the filtration area was the same to maintain a similar pressure drop across the filter walls. With these assumptions, square and triangle channels resulted in having the same hydraulic diameter and wall Reynolds number, which could be compared directly as depicted in Figure 11.13 (a). It should be noted that hexagon channels might create additional difficulties for any comparison, since are configured in a 2:1 inlet to outlet ratio, and might also require a choice of flow symmetry, if the flow uses all the inlet channels walls or only uses half of the available channels' areas, or even something intermediate. With these constraints, the hydraulic diameter of hexagon channels could differ from the square and triangle ones, making a comparison using the wall Reynolds number Re_w meaningless. It was shown in Wang and Bissett [44] that the ratio of w and D_h is a function of wS_f, although the function form is slightly different for the hexagon channel monolith compared to the triangle and square monoliths. A typical value of $wS_F = 0.15$ was chosen for the quantitative comparison and the resulting friction factors are plotted in Figure 11.13 (b) against an alternative parameter, the ratio between wW over μA_F, which are the same across the analyzed geometries.
Within the limitations of the comparison defined above, Figures 11.13 (b) ranks the geometries from triangle best (lowest $C_f Re$) to symmetric hexagon worst for lower flow rates. However, for higher flow rates, the symmetric hexagon catches up to and surpasses the square geometry, which is not the case if the comparison were made at the same Re_w as in Figure 11.13 (a). This demonstrates that "best geometry" questions are seldom easily answered and require precise definition of other conditions to be maintained during variation of the geometry.

The modeling of WFMs especially the catalyzed WFMs is complicated as it involves a multitude of physicochemical processes. The purpose of this chapter is to update the readers the most recent development in the 1D modeling of catalyzed or non-catalyzed WFMs. For the detailed modeling approaches for each process such as particle matter filtration, particle number and mass distribution, ash generation and transport, heat and mass transfer, reactions and the interaction of

these processes, the interested reader could refer to the references enclosed at the end of this chapter.
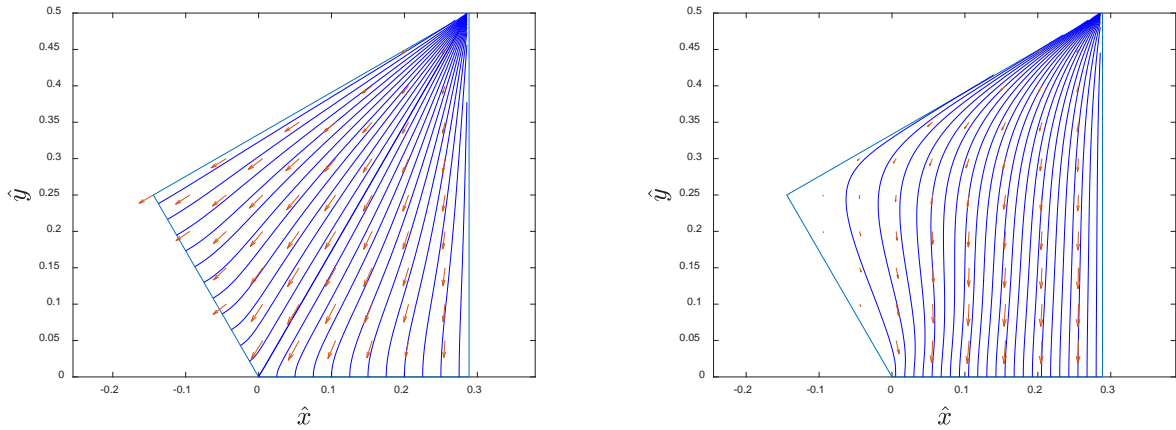

Figure 11.11: Streamlines in hexagon channels with suction ($\mathrm{Re}_w = 3$). (a) Symmetric BCs (b) symmetric BCs
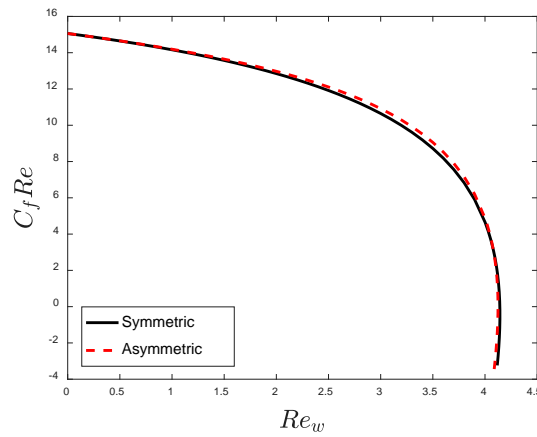

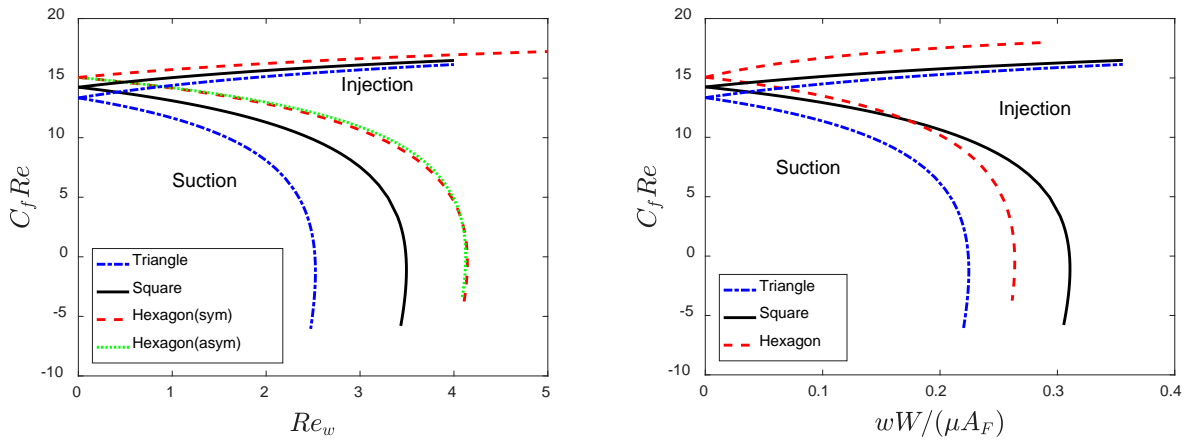Figure 11.12: Friction coefficient comparison in hexagon channels with suction

Figure 11.13: Friction coefficient comparison for different geometries vs Re number (a) and $wW/(\mu A_F)$ (b)

Table 11.2: (Wang and Bissett, [44]) Polynomial fitting functions for the triangle channel

$C_f Re$	Suction ($Re_w \leq 2$)	$C_f Re = 13.34 - 1.50 Re_w + 0.220 Re_w^2 - 0.387 Re_w^3$
	Injection ($Re_w \leq 4$)	$C_f Re = 13.34 + 1.12 Re_w - 0.108 Re_w^2$
β	Suction ($Re_w \leq 2$)	$\beta = 1.43 + 0.0180 Re_w + 0.0497 Re_w^2$
	Injection ($Re_w \leq 4$)	$\beta = 1.43 - 0.0253 Re_w$
Nu	Suction ($Re_w \leq 2$)	$Nu = 2.49 + 0.591 Pe_w - 0.166 Re_w$
	Injection ($Re_w \leq 4$)	$Nu = 2.49 - 0.400 Pe_w + 0.0189 Pe_w^2$

Table 11.3: (Bissett et al., [48]) Polynomial fitting functions for the square channel

$C_f Re$	Suction ($Re_w \leq 3$)	$C_f Re = 14.24 - 1.46 Re_w + 0.56 Re_w^2 - 0.27 Re_w^3$
	Injection ($Re_w \leq 3$)	$C_f Re = 14.24 + 0.83 Re_w - 0.07 Re_w^2$
β	Suction ($Re_w \leq 3$)	$\beta = 1.38 + 0.006 Re_w + 0.023 Re_w^2$
	Injection ($Re_w \leq 3$)	$\beta = 1.35 - 0.018 Re_w$
Nu	Suction ($Re_w \leq 3$)	$Nu = 2.98 + 0.60 Pe_w - 0.143 Re_w$
	Injection ($Re_w \leq 3$)	$Nu = 2.98 - 0.40 Pe_w$

Table 11.4: (Wang and Bissett, [44]) Polynomial fitting functions for the hexagon channel

$C_f Re$	Suction ($Re_w \leq 3.5$)	$C_f Re = 15.06 - 0.965 Re_w + 0.166 Re_w^2 - 0.114 Re_w^3$
	Injection ($Re_w \leq 9$)	$C_f Re = 15.06 + 0.609 Re_w - 0.0330 Re_w^2$
β	Suction ($Re_w \leq 3.5$)	$\beta = 1.35 + 0.0051 Re_w + 0.0135 Re_w^2$
	Injection ($Re_w \leq 9$)	$\beta = 1.35 - 0.00923 Re_w$
Nu	Suction ($Re_w \leq 3.5$)	$Nu = 3.34 + 0.605 Pe_w - 0.126 Re_w$
	Injection ($Re_w \leq 9$)	$Nu = 3.34 - 0.437 Pe_w + 0.0166 Pe_w^2$

Table 11.5: (Wang and Bissett, [44]) Limit point function fittings for the triangle channel

$C_f Re$	$-2.3 \le Re_w^s \le 4$	$C_f Re = (0.0457 + \dfrac{0.0519}{(Re_w^s + 2.52)^{0.621}})^{-1}$
β	$-2.3 \le Re_w^s \le 4$	$\beta = 1.04 + \dfrac{0.524}{(Re_w^s + 2.52)^{0.295}}$
Nu	$-2.3 \le Re_w^s \le 0$	$Nu = 2.49 - (0.600 Re_w^s - 0.380 Pe_w^s)(1 - \dfrac{1}{(Re_w^s + 2.52)^{0.113}})$ $-0.434 Pe_w^s Pr^{0.550}$
	$0 \le Re_w^s \le 4$	$Nu = 2.49 - 0.400 Pe_w^s + 0.0189(Pe_w^s)^2$

Table 11.6: (Wang and Bissett, [44]) Limit point function fitting functions for the square channel

$C_f Re$	$-3.4 \le Re_w^s \le 4$	$C_f Re = (0.0447 + \dfrac{0.0562}{(Re_w^s + 3.49)^{0.628}})^{-1}$
β	$-3.4 \le Re_w^s \le 4$	$\beta = 0.639 + \dfrac{0.885}{(Re_w^s + 3.49)^{0.136}}$
Nu	$-3.4 \le Re_w^s \le 0$	$Nu = 2.98 - (0.233 Re_w^s - 0.176 Pe_w^s)(1 - \dfrac{1}{(Re_w^s + 3.49)^{0.171}})$ $-0.466 Pe_w^s Pr^{0.451}$
	$0 \le Re_w^s \le 4$	$Nu = 2.98 - 0.429 Pe_w^s + 0.0165(Pe_w^s)^2$

Table 11.7: (Wang and Bissett, [44]) Limit point function fittings for the hexagon channel

$C_f Re$	$-4 \le Re_w^s \le 9$	$C_f Re = (0.0449 + \dfrac{0.0525}{(Re_w^s + 4.14)^{0.626}})^{-1}$
β	$-4 \le Re_w^s \le 9$	$\beta = 0.984 + \dfrac{0.504}{(Re_w^s + 4.14)^{0.215}}$
Nu	$-4 \le Re_w^s \le 0$	$Nu = 3.34 - (0.0855 Re_w^s - 0.0739 Pe_w^s)(1 - \dfrac{1}{(Re_w^s + 4.14)^{0.405}})$ $-0.483 Pe_w^s Pr^{0.403}$
	$0 \le Re_w^s \le 9$	$Nu = 3.34 - 0.437 Pe_w^s + 0.0166(Pe_w^s)^2$

11.4 Measurements and Model Calibration

Reactions play such an important role in the modeling of AT reactors that the majority of the papers published in the literature are focused on the development of kinetic mechanisms for different catalysts. Physical processes in monoliths are reasonably well understood but currently there is no theory available that can reasonably predict the kinetics for a given catalyst. Currently measurements are the only way to reliably measure the kinetics. Kinetics mechanisms are usually divided into micro kinetics and global kinetics. With a micro kinetics approach, all the reactions sub-steps are detailed and modeled, which often requires a significant calibration effort, due to the large number of variables involved, and a deep understanding of the kinetics, which could be only obtained by means of an extensive laboratory-scale characterization. A global kinetic approach instead does not consider all the elementary steps behind each reaction, thus reducing the calibration effort required and the complexity of the problem. For this reason, global kinetics mechanisms are predominantly used in the aftertreatment community. In this respect it is often prudent to take a minimalistic view and, therefore, start with simplest mechanism that fits a given class of catalyst. Subsequently experimental results can be used to refine the global kinetic model to fit the observation. Experiments are usually carried out on small monolith samples extracted from larger monoliths provided by the monolith suppliers. Samples can be commercially pre-washcoated or can be washcoated in-house if testing new catalyst formulations. Synthetic gases are used, hence the name SGB test bench, to simulate the exhaust from a real engine. A simple SGB scheme is depicted in Figure 11.14, related to ammonia storage experiments on LNT samples. The gas flow rates in SGBs is selected such that space velocity is the same as full scale system (i.e. residence time of the gas inside the channel same for both SGB and full-scale system). This minimizes the amount of synthetic gases used and hence the cost of the experiments.
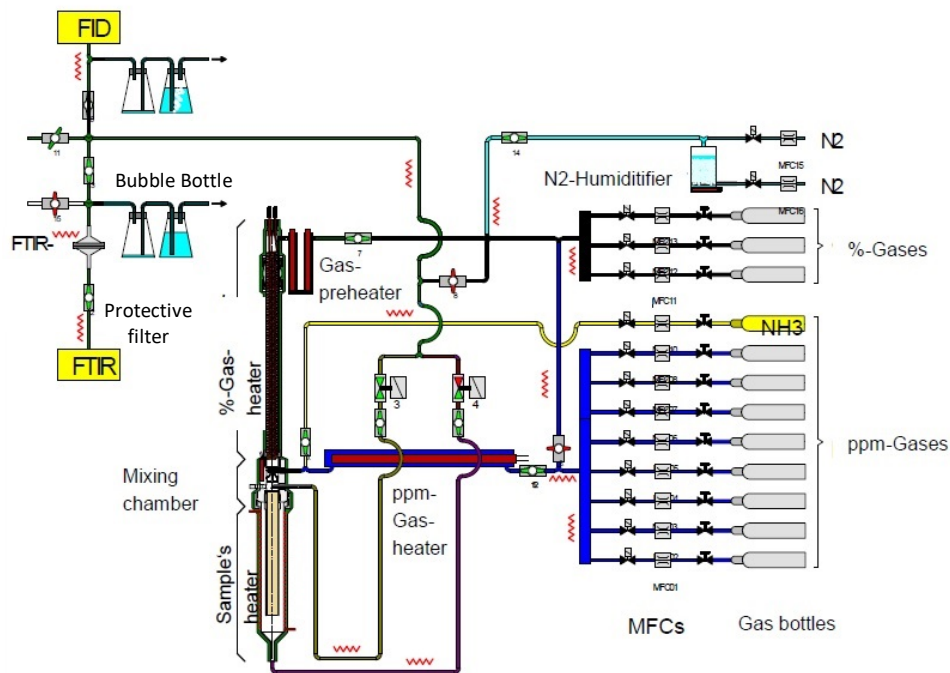

Figure 11.14 Experimental setup: schematic view of laboratory gas bench [4]

It is important to note that these laboratory (synthetic gas bench or SGB) tests has to be very carefully designed such that some important criteria are met:

a) The stoichiometry of the mixture should be representative of the application of full-scale reactors
b) The different batches of mixture for each experiment should be designed (as much as possible) to explore the behavior of smallest subset of the mechanism
c) The space velocity and temperature ranges should be chosen in commensurate with full-scale reactor
d) Finally, inlet conditions should be also be chosen such that the conversion efficiencies are far away from 0 and 100% such that as much of kinetic information can be extracted as possible.

With these criteria in mind, the so called SGB test protocols are designed and, perhaps refined based on the observation. As an example, the LNT test protocol used in Ref [4] is detailed in Table 11.8.

Table 11.8: Test protocol to characterize LNT operations by means of SGB experiments [4]

Characteristic	Test Protocol	Inlet Reductant Feed
Light Off	*A temperature ramp, from 100 to 500 °C, rate ≤5 °C/min, is applied to the sample in order to charcterize HC, CO and NO oxidation*	*H2* *CO* *HC (Propylene, Xylene, Dodecane)*
NOx Storage	*Temperature Programmed Desorption: an isothermal NOx loading window is followed by a temperature ramp up to 500°C where stored NOx are released*	
NOx Reduction	*lean/rich cycling test are performed in order to observe NOx storage (lean phase) and reduction (rich purge)*	*H2* *CO* *HC (Propylene)*
Oxygen Storage Capacity	*Lean/rich cycling tests are performed in order to characterize oxygen storage during the lean phase and HCs oxidation during the rich purge*	*H2* *CO* *HC (Propylene)*

Each experiment must be designed to characterize a particular catalyst operation. As an example, a scheme for light-off, Temperature Programmed Desorption (TPD) and NOx Storage and Reduction experiments is depicted in Figure 11.15.
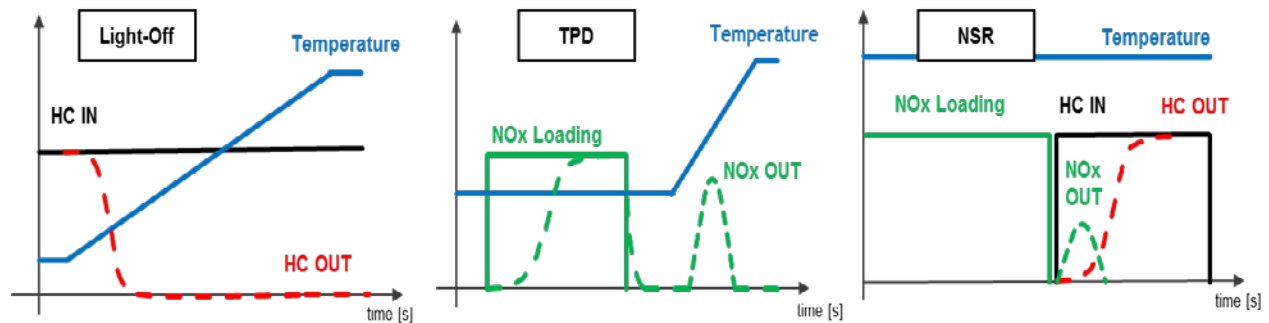
Figure 11.15: sample of tests protocols for Light-off, TPD and NSR experiments

It should be noted that such protocols may need to be revised based on the formulation of the catalyst and existing knowledge base.

Ideally kinetics measured in SGB test should be used in full scale system without any modification of the reaction rate parameters, but it is often found that the model predictions do not agree with full scale experiments. One of the primary reasons for the departure is due to small number of HC species used in the SGB tests whereas there is a wide spectrum of HC in the engine out exhaust gas. There are secondary reasons such as entrance effects, when heat and mass dispersion effects are significant, similarity in scale up may be compromised [49]. This necessitates the adjustments of kinetics for using in full scale system.

11.5 Models for Controls

Map-based models traditionally used in ECUs require great calibration effort to accurately represent the physics over the whole operating range of an engine and hence physics-based models are highly desirable for control purpose. Physics-based models can also estimate difficult/impossible to measure variables such as NH_3 storage [50] but, due to the highly non-linear reaction source terms, even a 1D single channel simulation would require a lot of computing power (CPU speed and memory) making this approach inappropriate for certain applications [51]. For effective control of aftertreatment systems in automobiles and commercial vehicles, one of the main challenges lies in the limited computing power that resides within the Engine Control Unit (ECU). ECU needs a plant model, among other things, for feedback control of DEF dosing, DPF/GPF regeneration and electrical heating strategies. Traditionally, these models are so called linearized models which are preferred by control engineers due to the well-developed linear control theories that can be readily adapted for designing optimum control systems [51]. However, linear models are not accurate over the whole operating regions and often not physics-based (e.g. is a fit of experimental data). On the other hand, it may be possible to construct simplified physical models of aftertreatment components, called grey-box models, able to deliver high level of accuracy over a wider range of operating conditions, while limiting the computational effort within the constraints of the limited resources in the ECU. One more attractive property of the grey-box models is that the equations are in such a form that they can be linearized without much effort. In this case, the accuracy of linear models might be limited to a small region around the operating point from where the linearized response function is created. However, one possible solution to this problem could be to develop multiple piecewise linear plant models, thus delivering sufficient accuracy for the entire operating range of the SCR. In

this case, the controller algorithm should perform the following main steps at each sample: (i) identifies the active linear model based on the values of the exogenous input signals, (ii) measures outputs and estimates the states using a state observer for the selected linear model (iii) calculates the control law that has been designed for the specific operating area.

There are many control-oriented models presented in the literature and the level of physical details included in those models may vary significantly. Gundlapally et al. [52] recently proposed a systematic procedure for developing grey-box models from detailed models. It is shown that the grey-box model includes all qualitative features of the detailed model and the parameters used in the grey-box model are closely related to the detailed model it is derived from. McMackin et al. [50] presented a SCR grey-box model similar to the one presented by Gundlapally et al. [52] but with an expanded set of reactions. The model was compared with the detailed model over 200 points covering entire operating map of a diesel engine. Figure 11.16 shows the comparison of NH_3 storage and NOx output predicted from both the grey-box model and detailed model for 34000 s of simulation.

In order to implement the grey-box model on the ECU, it needs to be compiled into a machine language and flashed (embedded) into the ECU. McMackin et al. [50] imbedded the SCR grey-box model onto a Bosch ECU (ES910) for the purpose of studying various urea control dosing strategies. They reported that grey-box model predictions match, with a limited calibration effort, their existing ECU code performance, which uses map-based models instead. Also, as shown in Figure 11.17, considerable improvements can be achieved with respect to engine out NOx, N_2O and NH_3 slippage based on strategies that maintain an optimum coverage state of the SCR (θ), as predicted by the embedded grey-box model.

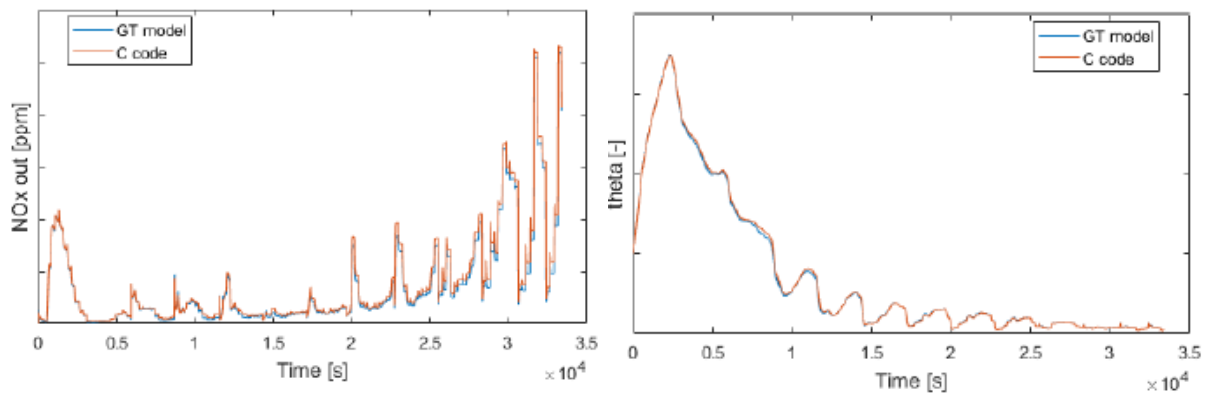*Figure 11.16: SCR grey-box model for controls applications. NOx emissions over driving cycle comparison: 1+1D Model (GT model) vs. grey-box model (C code) (left-hand side image). Fractional coverage of NH3 storage sites (theta): 1+1D Model (GT model) vs. grey-box model (C code) (right-hand side image) [50]*
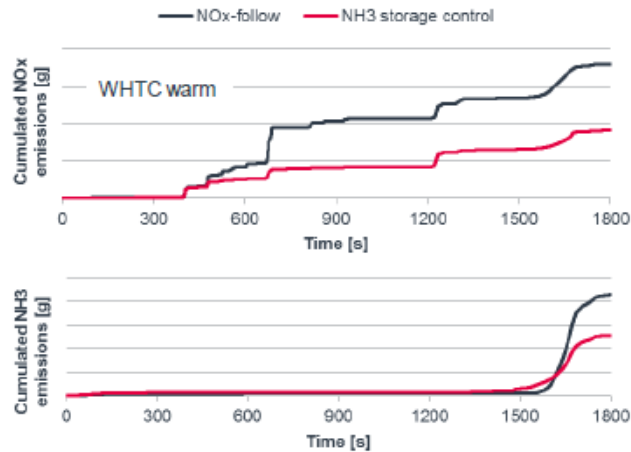
Figure 11.17: SCR grey-box model for controls applications. NOx emissions (top image) and ammonia slip (bottom image) comparison between the ECU NO_x-follow control strategy and the grey-box based NH_3-storage control strategy [50]

11.6 Concluding Remarks

More stringent emissions standards are being adopted worldwide due to a growing concern about pollution effects on the environment and human health. In this context, the aftertreatment systems play an essential role in both spark and compression ignition engines.

To comply with the new emissions regulations, compression ignition engines require the combination of different aftertreatment devices placed upstream in the exhaust line, as close as possible to the engine, to accelerate the warm up and to increase the operating temperature of the system. Therefore, modern exhaust aftertreatment systems for compression ignition include a great variety of architectures combining several devices such as a wall-flow particulate filter to collect the particulate matter, often integrated with an SCR coating for NOx abatement, and a series of flow-through monolithic reactors in charge for CO, HC and NOx low temperature storage and subsequent high temperature abatement.

In spark ignition engines, the introduction of direct injection has allowed an increase in the combustion efficiency thus reducing CO_2 emissions, although requiring the adoption of the wall-flow Gasoline Particulate Filter (GPF) to fulfill the regulation limits for particulate matter. Due to the stoichiometric operation conditions in spark ignition engines, the Three-Way Catalyst (TWC) can fulfill the simultaneous abatement of CO, HC and NOx emissions.

On the other side, upcoming standards are introducing more demanding test procedures, such as Real Driving Emissions (RDE), including more stringent durability requirements, in the form of deterioration factors, and severe low temperature tests. widening the boundary conditions under which the engine emissions must be carefully controlled. In this context, the automotive industry

demands flexible aftertreatment modelling tools which could play a crucial role in both the early engine design phase and in the final vehicle on-board applications.

Aim of the authors has been to support the aftertreatment community in such a challenging framework, providing an overview of the state of the art in the aftertreatment modeling as well as examples of real-world applications.

In this chapter, after a first description of the principal catalyst technologies used in aftertreatment components, a deep insight in modeling techniques has been given, both for flow through and for wall flow monoliths. Main hypotheses have been described and governing equations have been presented, covering different AT design options. Different modeling approaches have been analyzed, including detailed physics-based models, which are mainly used in the exhaust aftertreatment design and development phase, as well as reduced order models, which combine the physics-based accuracy with the reduced computational effort, making such models suitable for direct integration on the vehicle, for On-Board Diagnostics (OBD) and emissions control applications. Practical examples have been included and the approach to experimental measurements for modeling purpose has been analyzed.

References

1.   Merker, G.P., Schwarz, C., and Teichmann, R., eds., "Combustion Engines Development," Springer Berlin Heidelberg, Berlin, Heidelberg, ISBN 978-3-642-02951-6, 2012, doi:10.1007/978-3-642-14094-5.

2.   Ronald M. Heck, Robert J. Farrauto, S.T.G., "'Catalytic Air Pollution Control: Commercial Technology', 3rd Edition," 3rd ed., ISBN 978-0-470-27503-0, 2016.

3.   Millo, F., Rafigh, M., Sapio, F., Barrientos, E.J., and Ferreri, P., "Application of Genetic Algorithm for the Calibration of the Kinetic Scheme of a Diesel Oxidation Catalyst Model," 2018, doi:10.4271/2018-01-1762.

4.   Millo, F., Rafigh, M., Sapio, F., Wahiduzzaman, S., Dudgeon, R., Ferreri, P., and Barrientos, E., "Modeling NOx Storage and Reduction for a Diesel Automotive Catalyst Based on Synthetic Gas Bench Experiments," *Ind. Eng. Chem. Res.* 57(37):12335–12351, 2018, doi:10.1021/acs.iecr.8b01813.

5.   Millo, F., Rafigh, M., Andreata, M., Vlachos, T., Arya, P., and Miceli, P., "Impact of high sulfur fuel and de-sulfation process on a close-coupled diesel oxidation catalyst and diesel particulate filter," *Fuel* 1–10, 2017, doi:10.1016/j.fuel.2017.01.006.

6.   Colombo, M., Nova, I., Tronconi, E., Schmeißer, V., Bandl-Konrad, B., and Zimmermann, L., "Experimental and modeling study of a dual-layer (SCR+PGM) NH3 slip monolith catalyst (ASC) for automotive SCR aftertreatment systems. Part 1. Kinetics for the PGM component and analysis of SCR/PGM interactions," *Appl. Catal. B Environ.* 142–143:861–876, 2013, doi:10.1016/j.apcatb.2012.10.031.

7.   Opitz, B., Drochner, A., Vogel, H., and Votsmeier, M., "An experimental and simulation study on the cold start behaviour of particulate filters with wall integrated three way catalyst," *Appl. Catal. B Environ.* 144:203–215, 2014, doi:10.1016/j.apcatb.2013.06.035.

8.   Schejbal, M., Štěpánek, J., Marek, M., Kočí, P., and Kubíček, M., "Modelling of soot oxidation by NO2 in various types of diesel particulate filters," *Fuel* 89(9):2365–2375, 2010, doi:10.1016/j.fuel.2010.04.018.

9.   Koltsakis, G., Haralampous, O., Depcik, C., and Ragone, J.C., "Catalyzed diesel particulate filter modeling," *Rev. Chem. Eng.* 29(1):1–61, 2013, doi:10.1515/revce-2012-0008.

10. Kuo, J.C.W. and Lassen, H.G., "Mathematical Modeling of CO and HC Catalytic Converter Systems," SAE Technical Paper 710289, 1971," *SAE Tech. Pap. 710289\r* 1098–1125, 1971, doi:10.4271/710289.

11. Young, L.C. and Finlayson, B.A., "Mathematical Models of the Monolith Catalytic Converter," *AIChE J.* 22(2):331–344, 1976, doi:10.1002/aic.690220217.

12. Heck, R.H., Wei, J., and Katzer, J.R., "Mathematical modeling of monolithic catalysts," *AIChE J.* 22(3):477–484, 1976, doi:10.1002/aic.690220310.

13. Liu, Z.G. and Miller, R.K., "Flow Distributions and Pressure Drops of Wall-Flow Diesel Particulate Filters," *SAE 2002 World Congress & Exhibition*, SAE International, 2002, doi:https://doi.org/10.4271/2002-01-1311.

14. Payri, F., Arnau, F.J., Piqueras, P., and Ruiz, M.J., "Lumped Approach for Flow-Through and Wall-Flow Monolithic Reactors Modelling for Real-Time Automotive Applications," *WCX World Congress Experience*, SAE International, 2018, doi:https://doi.org/10.4271/2018-01-0954.

15. Konstandopoulos, A.G., Kostoglou, M., Vlachos, N., and Kladopoulou, E., "Progress in Diesel Particulate Filter Simulation," 2005, doi:10.4271/2005-01-0946.

16. Konstandopoulos, A.G., Kostoglou, M., Vlachos, N., and Kladopoulou, E., "Advances in the science and technology of diesel particulate filter simulation," 213–294, 2007, doi:10.1016/S0065-2377(07)33004-4.

17. Tronconi, E., Nova, I., Marchitti, F., Koltsakis, G., Karamitros, D., Maletic, B., Markert, N., Chatterjee, D., and Hehle, M., "Interaction of NO x Reduction and Soot Oxidation in a DPF with Cu-Zeolite SCR Coating," *Emiss. Control Sci. Technol.* 1(2):134–151, 2015, doi:10.1007/s40825-015-0014-y.

18. Gundlapally, S.R. and Balakotaiah, V., "Heat and mass transfer correlations and bifurcation analysis of catalytic monoliths with developing flows," *Chem. Eng. Sci.* 66(9):1879–1892, 2011, doi:10.1016/j.ces.2011.01.045.

19. Chapman, S., Cowling, T.G., Burnett, D., and Cercignani, C., "The Mathematical Theory of Non-uniform Gases: An Account of the Kinetic Theory of Viscosity, Thermal Conduction and Diffusion in Gases," Cambridge University Press, ISBN 9780521408448, 1990.

20. Fuller, E.N., Schettler, P.D., and Giddings, J.C., "NEW METHOD FOR PREDICTION OF BINARY GAS-PHASE DIFFUSION COEFFICIENTS," *Ind. Eng. Chem.* 58(5):18–27, 1966, doi:10.1021/ie50677a007.

21. Bird, R.B., Stewart, W.E., and Lightfoot, E.N., "Transport Phenomena," ISBN 0471410772, 2007, doi:10.1016/j.ijhydene.2006.08.059.

22. Zhang, F., Hayes, R.E., and Kolaczkowski, S.T., "A New Technique to Measure the Effective Diffusivity in a Catalytic Monolith Washcoat," *Chem. Eng. Res. Des.* 82(4):481–489, 2004, doi:10.1205/026387604323050191.

23. Wurzenberger, J.C. and Wanker, R., Multi-Scale SCR Modeling, 1D Kinetic Analysis and 3D System Simulation, *SAE Tech. Pap.*, 2005, doi:10.4271/2005-01-0948.

24. Metkar, P.S., Harold, M.P., and Balakotaiah, V., "Experimental and kinetic modeling study of NH3-SCR of NOx on Fe-ZSM-5, Cu-chabazite and combined Fe- and Cu-zeolite monolithic catalysts," *Chem. Eng. Sci.* 87(x):51–66, 2013, doi:10.1016/j.ces.2012.09.008.

25. Václavík, M., Kočí, P., Novák, V., and Thompsett, D., "NOx conversion and selectivity in multi-layer and sequential DOC-LNT automotive exhaust catalysts: Influence of internal transport," *Chem. Eng. J.* 329:128–134, 2017, doi:10.1016/j.cej.2017.05.129.

26. Scheuer, A., Hauptmann, W., Drochner, A., Gieshoff, J., Vogel, H., and Votsmeier, M., "Dual layer automotive ammonia oxidation catalysts: Experiments and computer simulation," *Appl. Catal. B Environ.* 111–112:445–455, 2012, doi:10.1016/j.apcatb.2011.10.032.

27. Aris, R., "The Mathematical Theory of Diffusion and Reaction in Permeable Catalysts: Vol. 1: The Theory of the Steady State (Oxford Studies in Physics)," 1975.

28. Joshi, S.Y., Harold, M.P., and Balakotaiah, V., "Overall mass transfer coefficients and controlling regimes in catalytic monoliths," *Chem. Eng. Sci.* 65(5):1729–1747, 2010, doi:10.1016/j.ces.2009.11.021.

29. Balakotaiah, V., "On the relationship between Aris and Sherwood numbers and friction and effectiveness factors," *Chem. Eng. Sci.* 63(24):5802–5812, 2008, doi:10.1016/j.ces.2008.08.025.

30. Mozaffari, B., Tischer, S., Votsmeier, M., and Deutschmann, O., "A one-dimensional modeling approach for dual-layer monolithic catalysts," *Chem. Eng. Sci.* 139:196–210, 2016, doi:10.1016/j.ces.2015.09.021.

31. Bissett, E.J., "An Asymptotic Solution for Washcoat Pore Diffusion in Catalytic

Monoliths," *Emiss. Control Sci. Technol.* 1(1):3–16, 2015, doi:10.1007/s40825-015-0010-2.

32. Bissett, E.J., "Small washcoat diffusion resistance, further developments," *CLEERS Workshop*, Dearborn, USA, 2015.

33. Gundlapally, S.R., Dudgeon, R., and Wahiduzzaman, S., "Efficient Solution of Washcoat Diffusion-Reaction Problem for Real-Time Simulations," *Emiss. Control Sci. Technol.* 4(2):90–102, 2018, doi:10.1007/s40825-018-0083-9.

34. Gundlapally, S.R., "Effect of non-uniform activity and conductivity on the steady-state and transient performance of catalytic reactors," University of Houston, 2011.

35. Oh, S.H., Bissett, E.J., and Battiston, P.A., "Mathematical modeling of electrically heated monolith converters: model formulation, numerical methods, and experimental verification," *Ind. Eng. Chem. Res.* 32(8):1560–1567, 1993, doi:10.1021/ie00020a005.

36. Bissett, E.J., "Mathematical model of the thermal regeneration of a wall-flow monolith diesel particulate filter," *Chem. Eng. Sci.* 39(7–8):1233–1244, 1984, doi:10.1016/0009-2509(84)85084-8.

37. Konstandopoulos, A.G. and Johnson, J.H., "Wall-Flow Diesel Particulate Filters—Their Pressure Drop and Collection Efficiency," 1989, doi:10.4271/890405.

38. Haralampous, O.A. and Koltsakis, G.C., "Oxygen diffusion modeling in diesel particulate filter regeneration," *AIChE J.* 50(9):2008–2019, 2004, doi:10.1002/aic.10181.

39. Haralampous, O.A. and Koltsakis, G.C., "Back-Diffusion Modeling of NO 2 in Catalyzed Diesel Particulate Filters," *Ind. Eng. Chem. Res.* 43(4):875–883, 2004, doi:10.1021/ie034187p.

40. Kandylas, I.P. and Koltsakis, G.C., "NO 2 -Assisted Regeneration of Diesel Particulate Filters: A Modeling Study," *Ind. Eng. Chem. Res.* 41(9):2115–2123, 2002, doi:10.1021/ie010842m.

41. Bissett, E.J. and Wang, W., "On the Implications of Wall Reynolds Number Dependent Nusselt Number and Friction Factor on the Accuracy of Wall - Flow DPF Modeling," *ModeGat III*, 2013.

42. Bissett, E.J., Kostoglou, M., and Konstandopoulos, A.G., "Frictional and heat transfer characteristics of flow in square porous tubes of wall-flow monoliths," *Chem. Eng. Sci.* 84:255–265, 2012, doi:10.1016/j.ces.2012.08.012.

43. Koltsakis, G.C. and Stamatelos, A.M., "Modes of Catalytic Regeneration in Diesel Particulate Filters," *Ind. Eng. Chem. Res.* 36(10):4155–4165, 1997, doi:10.1021/ie970095m.

44. Wang, W. and Bissett, E.J., "Frictional and Heat Transfer Characteristics of Flow in Triangle and Hexagon Channels of Wall-Flow Monoliths," *Emiss. Control Sci. Technol.* 4(3):198–218, 2018, doi:10.1007/s40825-018-0093-7.

45. Iwasaki, K., "Innovative Aluminum Titanate Based - Diesel Particulate Filter Having Asymmetric Hexagonal Cell Geometry," 1–10, 2012, doi:10.4271/2012-01-0838.

46. Zhao, C., Zhu, Y., Wang, Y., and Huang, S., "Pressure Drop and Soot Regeneration Characteristics through Hexagonal and Square Cell Diesel Particulate Filters," *SAE Tech. Pap.* (March), 2017, doi:10.4271/2017-01-0979.

47. Tsuneyoshi, K. and Yamamoto, K., "Experimental study of hexagonal and square diesel particulate fi lters under controlled and uncontrolled catalyzed regeneration," *Energy* 60:325–332, 2013, doi:10.1016/j.energy.2013.07.069.

48. Bissett, E.J., Kostoglou, M., and Konstandopoulos, A.G., "Frictional and heat transfer

characteristics of flow in square porous tubes of wall-flow monoliths," *Chem. Eng. Sci.* 84:255–265, 2012, doi:10.1016/j.ces.2012.08.012.

49.   Gu, T. and Balakotaiah, V., "Impact of heat and mass dispersion and thermal effects on the scale-up of monolith reactors," *Chem. Eng. J.* 284:513–535, 2016, doi:10.1016/j.cej.2015.09.005.

50.   Mcmackin, M., "SCR model reduction process for physics-based ECU code," *GT European User Conference*, Frankfurt, 2017.

51.   Skaf, Z., Aliyev, T., Shead, L., and Steffen, T., "The State of the Art in Selective Catalytic Reduction Control," 2014, doi:10.4271/2014-01-1533.

52.   Gundlapally, S.R., Papadimitriou, I., Wahiduzzaman, S., and Gu, T., "Development of ECU Capable Grey-Box Models from Detailed Models---Application to a SCR Reactor," *Emiss. Control Sci. Technol.* 2(3):124–136, 2016, doi:10.1007/s40825-016-0039-x.